J. Fluid Mech. (2012), *vol.* 713, *pp.* 398–419. © Cambridge University Press 2012
doi:10.1017/jfm.2012.465

Drag reduction due to spatial thermal modulations

M. Z. Hossain‡, D. Floryan and J. M. Floryan†

Department of Mechanical and Materials Engineering, The University of Western Ontario, London, Ontario, N6A 5B9, Canada

(Received 31 December 2011; revised 24 July 2012; accepted 18 September 2012; first published online 26 October 2012)

It is demonstrated that a significant drag reduction for pressure-driven flows can be realized by applying spatially distributed heating. The heating creates separation bubbles that separate the stream from the bounding walls and, at the same time, alter the distribution of the Reynolds stress, thereby providing a propulsive force. The strength of this effect is of practical interest for heating with wavenumbers $\alpha = O(1)$ and for flows with small Reynolds numbers and, thus, it is of potential interest for applications in micro-channels. Explicit results given for a very simple sinusoidal heating demonstrate that the drag-reducing effect increases proportionally to the second power of the heating intensity. This increase saturates if the heating becomes too intense. Drag reduction decreases as α^4 when the heating wavenumber becomes too small, and as α^{-7} when the heating wavenumber becomes too large; this decrease is due to the reduction in the magnitude of the Reynolds stress. The drag reduction can reach up to 87 % for the heating intensities of interest and heating patterns corresponding to the most effective heating wavenumber.

Key words: drag reduction, flow control, low-Reynolds-number flows

1. Introduction

The reduction of drag associated with flows through channels is of practical importance, especially in the case of micro-channels where the required pressure drop may lead to significant forces acting on the bounding walls, resulting in structural problems. There are three mechanisms that contribute to the drag formation: the shear drag, the pressure form drag and the pressure interaction drag (Mohammadi & Floryan 2012). We shall focus this discussion on the reduction of the shear drag, with the tacit assumption that any increase of the pressure drag that may occur as a result of the shear-reducing efforts is negligible.

Four methods for shear reduction are available. The first relies on the so-called superhydrophobic effect (Rothstein 2010) and results from a combination of the hydrophobicity of the surface material and surface topography. When a superhydrophobic surface is submerged in a liquid, gas bubbles become trapped in surface micro-pores, effectively reducing the shear stress experienced by the liquid, as shear between the liquid and the solid is replaced by shear between the liquid and the

† Email address for correspondence: mfloryan@eng.uwo.ca

‡ Present address: Department of Mechanical Engineering, Bangladesh University of Engineering and Technology (BUET), Dhaka-1000, Bangladesh.

https://doi.org/10.1017/jfm.2012.465 Published online by Cambridge University Press

gas. Most of the available data relate to motion of water with bubbles of air forming in surface pores, with the research being inspired by the unique water-repellent properties of the lotus leaf (Barthlott & Neinhuis 1977). The drag-reducing ability can be increased by correct shaping of the surface pores/roughness (Samaha, Tafreshi & Gad-el-Hak 2011) and by increasing hydrophobicity through changes in surface chemistry (Gao & McCarthy 2006; Quéré 2008; Reyssat, Yeomans & Quéré 2008; Xi *et al.* 2008; Zhou *et al.* 2011). The laminar drag reduction due to superhydrophobic effects has been demonstrated both theoretically and experimentally (Ou, Perot & Rothstein 2004; Ou & Rothstein 2005; Joseph *et al.* 2006; Truesdell *et al.* 2006). Recent results point to the potential for drag reduction in turbulent flows (Daniello, Waterhouse & Rothstein 2009; Martell, Perot & Rothstein 2009).

The superhydrophobic effect requires the presence of two immiscible fluids, typically two phases, as shear between the main fluid and the bounding wall is replaced by shear between the main fluid and the less viscous secondary fluid. The superhydrophobic effect does not exist in the case of gas flows. The contributions of various forms of pressure drag to the overall drag of superhydrophobic surfaces is not known.

The second potential drag-reducing effect is associated with the rearrangement of the bulk flow through properly structured surface grooves (Mohammadi & Floryan 2011). The overall shear decreases in spite of an increase of the wetted area. The third effect is related to the use of extremely thin grooves with friction decreasing the flow velocity inside such grooves and, thus, reducing the shear to which the bounding wall is exposed (Mohammadi & Floryan 2011). Again, the overall shear decreases in spite of an increase of the wetted area. The fourth effect is associated with grooves specially structured for the creation of small separation bubbles where the fluid slows down, exposing the bounding wall to a reduced shear (Mohammadi & Floryan 2011). The last three effects are active in single-fluid systems.

The common characteristic of all of the methods described above is the use of special surface topography that leads to the formation of the desired flow structures. The purpose of this work is to demonstrate the existence of a drag-reducing effect that is independent of surface topography. This effect is created by an externally imposed spatially modulated heating. The correct pattern of heating–cooling creates a field of buoyancy force that leads to the formation of separation bubbles that isolate the main stream from direct contact with the bounding walls and, in this way, reduces shear. This effect, which had been referred to as the superthermohydrophobic effect (Floryan 2012), remains effective for very small Reynolds numbers, since stronger flows wash the separation bubbles away, and, thus, it is of interest for applications in micro-channels. All the results presented are for the Prandtl number $Pr = 0.71$ (air) to demonstrate the level of drag reduction that can be achieved in gases.

The mechanics of the drag-reducing effect is described using a simple model problem discussed in § 2. The solution method is described in § 3. Flow patterns are discussed in § 4. Pressure losses are analysed in § 5. The mechanics of drag reduction are discussed in § 6. Section 7 provides a short summary of the main conclusions.

2. Problem formulation

Consider steady flow of fluid confined in a channel bounded by two parallel walls extending to $\pm\infty$ in the x-direction and placed at a distance $2h$ apart with the gravitational acceleration g acting in the negative y-direction, as shown in figure 1. The flow is driven in the positive x-direction by a pressure gradient. The fluid is

https://doi.org/10.1017/jfm.2012.465 Published online by Cambridge University Press

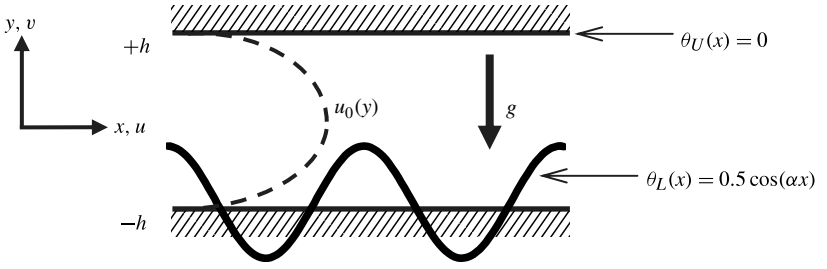


FIGURE 1. Sketch of the system configuration.

incompressible and Newtonian with thermal conductivity k, specific heat c, thermal diffusivity $\kappa = k/\rho c$, kinematic viscosity ν, dynamic viscosity μ, thermal expansion coefficient Γ and variations of the density ρ that follow the Boussinesq approximation. The lower wall is subject to periodic heating resulting in wall temperatures in the form

$$\theta_L(x) = \cos(\alpha x)/2, \quad \theta_U(x) = 0, \tag{2.1}$$

where θ denotes the relative temperature scaled with the amplitude of the peak-to-peak temperature variations along the lower wall T_d, i.e. $\theta = (T - T_U)/T_d$, T denotes the absolute temperature, $\lambda = 2\pi/\alpha$ is the wavelength of the heating, subscripts L and U refer to the lower and upper walls, respectively, and the channel half-height h has been used as the length scale.

The velocity and pressure fields in the absence of the heating have the form

$$\boldsymbol{v}_0(x, y) = [u_0(y), 0] = [1 - y^2, 0], \quad p_0(x, y) = -2x/Re \tag{2.2}$$

where $\boldsymbol{v}_0 = (u_0, v_0)$ denotes the velocity vector scaled with the maximum of the x-velocity U_{max}, p_0 stands for the pressure scaled with ρU_{max}^2 and the Reynolds number is defined as $Re = U_{max}h/\nu$.

The applied heating produces flow modifications that can be represented in the form

$$u_2(x, y) = Reu_0(y) + u_1(x, y), \quad v_2(x, y) = v_1(x, y), \tag{2.3a}$$

$$\theta_2(x, y) = Pr^{-1}\theta_0(x, y) + \theta_1(x, y), \quad p_2(x, y) = Re^2 p_0(x) + p_1(x, y). \tag{2.3b}$$

In the above, (u_2, v_2), p_2 and θ_2 denote the complete velocity, pressure and temperature fields, respectively, (u_1, v_1) and p_1 denote the velocity and pressure modifications created by the heating, respectively, θ_0 stands for the conductive temperature field and θ_1 denotes deviations from the conductive temperature field induced by the fluid motion. The complete velocity vector and the velocity modifications have been scaled using the convective velocity scale $U_v = \nu/h$ where $U_{max}/U_v = Re$, the pressure modifications have been scaled using ρU_v^2, and $T_v = T_d\nu/\kappa$ has been used as the convective temperature scale, where $T_v/T_d = Pr$ defines the Prandtl number. The maximum of θ_2 in this scaling is always $(2Pr)^{-1}$. The conductive temperature field θ_0 has the form

$$\left.\begin{aligned} &\theta_0(x, y) = \theta_0^{(1)}(y)\mathrm{e}^{\mathrm{i}\alpha x} + \theta_0^{(-1)}(y)\mathrm{e}^{-\mathrm{i}\alpha x}, \\ &\theta_0^{(1)}(y) = [-\sinh(\alpha y)/\sinh(\alpha) + \cosh(\alpha y)/\cosh(\alpha)]/8, \end{aligned}\right\} \tag{2.4}$$

https://doi.org/10.1017/jfm.2012.465 Published online by Cambridge University Press

where $\theta_0^{(-1)}$ is the complex conjugate of $\theta_0^{(1)}$. The field equations for the flow and temperature modifications have the form

$$(Reu_0 + u_1)\frac{\partial u_1}{\partial x} + Rev_1\frac{\mathrm{d}u_0}{\mathrm{d}y} + v_1\frac{\partial u_1}{\partial y} = -\frac{\partial p_1}{\partial x} + \nabla^2 u_1, \tag{2.5a}$$

$$(Re\,u_0 + u_1)\frac{\partial v_1}{\partial x} + v_1\frac{\partial v_1}{\partial y} = -\frac{\partial p_1}{\partial y} + \nabla^2 v_1 + Ra_p\theta_1 + Ra_pPr^{-1}\theta_0, \tag{2.5b}$$

$$Pr\left((Reu_0 + u_1)\frac{\partial \theta_1}{\partial x} + v_1\frac{\partial \theta_1}{\partial y}\right) + (Reu_0 + u_1)\frac{\partial \theta_0}{\partial x} + v_1\frac{\partial \theta_0}{\partial y} = \nabla^2\theta_1, \tag{2.5c}$$

$$\frac{\partial u_1}{\partial x} + \frac{\partial v_1}{\partial y} = 0, \tag{2.5d}$$

where $Ra_p = g\Gamma h^3 T_d/\nu\kappa$ is the Rayleigh number that measures the intensity of the heating and ∇^2 denotes the Laplace operator. The limit of $Re \to 0$ corresponds to pure convection. An increase of Re leads to modifications of convection by the imposed flow. The main interest is in the determination of the aperiodic part of the pressure modification p_1 as it provides information about the flow losses induced by the heating. The physical problem is posed as the question of finding the additional pressure gradient that is required in order to maintain the same flow rate in the heated and isothermal channels. The solution must therefore satisfy the flow rate constraint in the form

$$Q = \int_{-1}^{1} u_2\,\mathrm{d}y = \int_{-1}^{1} (Re\,u_0 + u_1)\,\mathrm{d}y = 4\,Re\,/3. \tag{2.6}$$

Elimination of the imposed flow corresponds to the limit $Re \to 0$. Elimination of the heating corresponds to the limit $Ra_p \to 0$ which results in $u_1 = v_1 = p_1 = \theta_1 = 0$ with the flow field being described by (2.2).

The problem formulation is closed by specifying the no-slip, the no-penetration and the thermal boundary conditions in the form

$$u_1(\pm 1) = 0, \quad v_1(\pm 1) = 0, \quad \theta_1(\pm 1) = 0. \tag{2.7}$$

Solution of (2.5)–(2.7) results in the simultaneous determination of the velocity and temperature fields, followed by the determination of the pressure field including the mean pressure gradient, which is of main interest.

3. Method of solution

We define the stream function $\psi(x, y)$ in the usual manner, i.e. $u_1 = \partial\psi/\partial y$, $v_1 = -\partial\psi/\partial x$ and eliminate pressure, bringing the governing equations to the form

$$Re\,u_0\frac{\partial}{\partial x}(\nabla^2\psi) - Re\frac{\mathrm{d}^2 u_0}{\mathrm{d}y^2}\frac{\partial\psi}{\partial x} + N_\psi = \nabla^4\psi - Ra_p\frac{\partial\theta_1}{\partial x} - Ra_pPr^{-1}\frac{\partial\theta_0}{\partial x}, \tag{3.1a}$$

$$Pr\,Re\,u_0\frac{\partial\theta_1}{\partial x} + Pr\,N_{\theta 1} + Re\,u_0\frac{\partial\theta_0}{\partial x} + N_{\theta 0} = \nabla^2\theta_1, \tag{3.1b}$$

where ∇^4 denotes the biharmonic operator, the nonlinear terms are written in the conservative form, i.e.

$$N_\psi = \frac{\partial}{\partial y}\left(\frac{\partial}{\partial x}\langle u_1u_1\rangle + \frac{\partial}{\partial y}\langle u_1v_1\rangle\right) - \frac{\partial}{\partial x}\left(\frac{\partial}{\partial x}\langle u_1v_1\rangle + \frac{\partial}{\partial y}\langle v_1v_1\rangle\right), \tag{3.2a}$$

https://doi.org/10.1017/jfm.2012.465 Published online by Cambridge University Press

$$N_{\theta 1} = \frac{\partial}{\partial x}\langle u_1\theta_1\rangle + \frac{\partial}{\partial y}\langle v_1\theta_1\rangle, \quad N_{\theta 0} = \frac{\partial}{\partial x}\langle u_1\theta_0\rangle + \frac{\partial}{\partial y}\langle v_1\theta_0\rangle, \tag{3.2b}$$

and $\langle\cdots\rangle$ denotes products. The solution is assumed to be in the form of Fourier expansions

$$\psi(x,y) = \sum_{n=-\infty}^{n=+\infty} \varphi^{(n)}(y)\,\mathrm{e}^{\mathrm{i}n\alpha x}, \quad \theta_1(x,y) = \sum_{n=-\infty}^{n=+\infty} \phi^{(n)}(y)\,\mathrm{e}^{\mathrm{i}n\alpha x}, \tag{3.3a,b}$$

$$u_1(x,y) = \sum_{n=-\infty}^{n=+\infty} u_1^{(n)}(y)\,\mathrm{e}^{\mathrm{i}n\alpha x}, \quad v_1(x,y) = \sum_{n=-\infty}^{n=+\infty} v_1^{(n)}(y)\,\mathrm{e}^{\mathrm{i}n\alpha x}, \tag{3.3c,d}$$

$$p_1(x,y) = Ax + \sum_{n=-\infty}^{n=+\infty} p_1^{(n)}(y)\,\mathrm{e}^{\mathrm{i}n\alpha x} \tag{3.3e}$$

where $u_1^{(n)} = \mathrm{D}\varphi^{(n)}$, $v_1^{(n)} = -\mathrm{i}n\alpha\varphi^{(n)}$, $\varphi^{(n)} = \varphi^{(-n)*}$, $u_1^{(n)} = u_1^{(-n)*}$, $v_1^{(n)} = v_1^{(-n)*}$, $p_1^{(n)} = p_1^{(-n)*}$, $*$ denotes the complex conjugate, and A stands for the streamwise pressure-gradient correction induced by the heating. Positive values of A correspond to drag reduction. The products are expressed using Fourier expansions in the form

$$\left.\begin{aligned} \langle u_1u_1\rangle &= \sum_{n=-\infty}^{n=+\infty} \langle u_1u_1\rangle^{(n)}(y)\,\mathrm{e}^{\mathrm{i}n\alpha x}, \quad \langle u_1v_1\rangle = \sum_{n=-\infty}^{n=+\infty} \langle u_1v_1\rangle^{(n)}(y)\,\mathrm{e}^{\mathrm{i}n\alpha x}, \\ \langle v_1v_1\rangle &= \sum_{n=-\infty}^{n=+\infty} \langle v_1v_1\rangle^{(n)}(y)\,\mathrm{e}^{\mathrm{i}n\alpha x}, \end{aligned}\right\} \tag{3.3f}$$

$$\left.\begin{aligned} \langle u_1\theta_1\rangle &= \sum_{n=-\infty}^{n=+\infty} \langle u_1\theta_1\rangle^{(n)}(y)\,\mathrm{e}^{\mathrm{i}n\alpha x}, \quad \langle v_1\theta_1\rangle = \sum_{n=-\infty}^{n=+\infty} \langle v_1\theta_1\rangle^{(n)}(y)\,\mathrm{e}^{\mathrm{i}n\alpha x}, \\ \langle u_1\theta_0\rangle &= \sum_{n=-\infty}^{n=+\infty} \langle u_1\theta_0\rangle^{(n)}(y)\,\mathrm{e}^{\mathrm{i}n\alpha x}. \end{aligned}\right\} \tag{3.3g}$$

Substitution of (3.3) into (3.1) and separation of Fourier components result in a system of ordinary differential equations for the modal functions for $-\infty < n < \infty$ in the form

$$\mathrm{D}_n^2\varphi^{(n)} - \mathrm{i}n\alpha\, Re\,(u_0\mathrm{D}_n - \mathrm{d}^2u_0/\mathrm{d}y^2)\varphi^{(n)} - \mathrm{i}n\alpha\, Ra_p\phi^{(n)} = \mathrm{i}n\alpha\, Ra_p\, Pr^{-1}\theta_0^{(n)} + N_\psi^{(n)}, \tag{3.4a}$$

$$\mathrm{D}_n\phi^{(n)} - \mathrm{i}n\alpha\, Pr\, Re\, u_0\phi^{(n)} = \mathrm{i}n\alpha\, Re\, u_0\,\theta_0^{(n)} + N_{\theta 0}^{(n)} + Pr\, N_{\theta 1}^{(n)} \tag{3.4b}$$

where

$$\left.\begin{aligned} &\mathrm{D} = \mathrm{d}/\mathrm{d}y,\ \mathrm{D}^2 = \mathrm{d}^2/\mathrm{d}y^2, \quad \mathrm{D}_n = \mathrm{D}^2 - n^2\alpha^2, \\ &N_{\theta 0}^{(n)} = \mathrm{i}n\alpha\langle u_1\theta_0\rangle^{(n)} + \mathrm{D}\langle v_1\theta_0\rangle^{(n)}, \quad N_{\theta 1}^{(n)} = \mathrm{i}n\alpha\,\langle u_1\theta_1\rangle^{(n)} + \mathrm{D}\langle v_1\theta_1\rangle^{(n)}, \\ &N_\psi^{(n)} = \mathrm{i}n\alpha\,\mathrm{D}\langle u_1u_1\rangle^{(n)} + \mathrm{D}^2\langle u_1v_1\rangle^{(n)} + \mathrm{i}n^2\alpha^2\langle u_1v_1\rangle^{(n)} - \mathrm{i}n\alpha\,\mathrm{D}\langle v_1v_1\rangle^{(n)}. \end{aligned}\right\} \tag{3.5}$$

The required boundary conditions for the modal functions have the form

$$\mathrm{D}\varphi^{(n)}(\pm 1) = 0, \quad \varphi^{(n)}(\pm 1) = 0, \quad \phi^{(n)}(\pm 1) = 0 \quad \text{for } -\infty < n < +\infty. \tag{3.6a–c}$$

System (3.4) together with the boundary and constraint conditions (3.6a–c) need to be solved numerically.

https://doi.org/10.1017/jfm.2012.465 Published online by Cambridge University Press

For the purpose of numerical solution, expansions (3.3) have been truncated after N_M terms. The discretization method uses the Chebyshev collocation technique based on N_T collocation points. The resulting nonlinear algebraic system of equations is solved using an iterative technique combined with under-relaxation in the form $\Phi_{j+1} = \Phi_j + RF(\Phi_{comp} - \Phi_j)$ where $\Phi = \{\varphi^{(n)}, \phi^{(n)}\}$ is the vector of unknowns, Φ_{comp} denotes the current solution, Φ_j denotes the previous solution, Φ_{j+1} stands for the accepted value of the next iteration and RF denotes the relaxation factor. The solution process starts with solution of (3.4) with the nonlinear terms on the right-hand side assumed to be zero; the first approximation of the nonlinear terms is computed on the basis of the available approximation of the velocity and temperature fields and the system (3.4) is resolved with the new approximation of the nonlinear terms used on the right-hand side. This process is continued until a convergence criterion in the form $\max(|\Phi_{comp} - \Phi_j|) < TOL$ is satisfied where TOL denotes the specified error. The number of collocation points and the number of Fourier modes used in the solution were selected through numerical experiments so that the flow quantities of interest were determined with at least six-digit accuracy. Typically $N_T = 50$ provided sufficient accuracy. The required value of N_M strongly depends on α, Re and Ra and can be as large as $N_M = 50$.

The evaluation of the nonlinear terms requires evaluation of products of two Fourier series. It is more efficient to evaluate these product in the physical rather than in the Fourier space. The required quantities were computed in the physical space on a suitable grid based on the collocation points in the y-direction and a uniformly distributed set of points in the x-direction, and the relevant products were evaluated. The fast Fourier transform (FFT) algorithm was used to express these products in terms of Fourier expansions (3.3*f*,*g*). The aliasing error was controlled using a discrete FFT transform with N_p rather than N_M points, where $N_p \geqslant 3N_M/2$.

The pressure field has been computed from the momentum equation. Insertion of (3.3) into (2.5*a*) and separation of Fourier modes leads to

$$p_1^{(n)} = \frac{1}{\mathrm{i}\, n\, \alpha}\left[(\mathrm{D}^2 - n^2\alpha^2 - \mathrm{i}n\alpha\, Re\, u_0)\,\mathrm{D}\varphi^{(n)} + \mathrm{i}n\alpha\, Re \frac{\mathrm{d}u_0}{\mathrm{d}y}\varphi^{(n)} - \mathrm{i}n\alpha\,\langle u_1 u_1\rangle - \mathrm{D}\langle u_1 v_1\rangle\right] \quad \text{for } n \neq 0, \tag{3.7a}$$

$$A = \mathrm{D}^3\varphi^{(0)} - \mathrm{D}\langle u_1 v_1\rangle^{(0)} \quad \text{for } n = 0. \tag{3.7b}$$

Equation (3.7*b*) has been used for determination of the additional pressure gradient A required to maintain the same flow in the heated channel as in the unheated one. Equation (3.7*a*) has been used to compute $p_1^{(n)}$, $n \neq 0$. The y-momentum equation has been used for determination of $p_1^{(0)}$; substitution of (3.3) into (2.5*b*), extraction of mode zero and integration between the two walls results in

$$p_1^{(0)} = Ra_p \int_{-1}^{y} \phi^{(0)}\,\mathrm{d}y - \langle v_1 v_1\rangle^{(0)} + \text{constant}. \tag{3.8}$$

4. Flow patterns

The flow pattern created by the heating in the absence of any net horizontal flow ($Re = 0$) is shown in figure 2(*a*). The flow topology is made up of pairs of counter-rotating rolls with the fluid moving upwards above the hot spots and is referred to as the type 1 topology. The corresponding temperature field illustrated in figure 2(*b*)

https://doi.org/10.1017/jfm.2012.465 Published online by Cambridge University Press

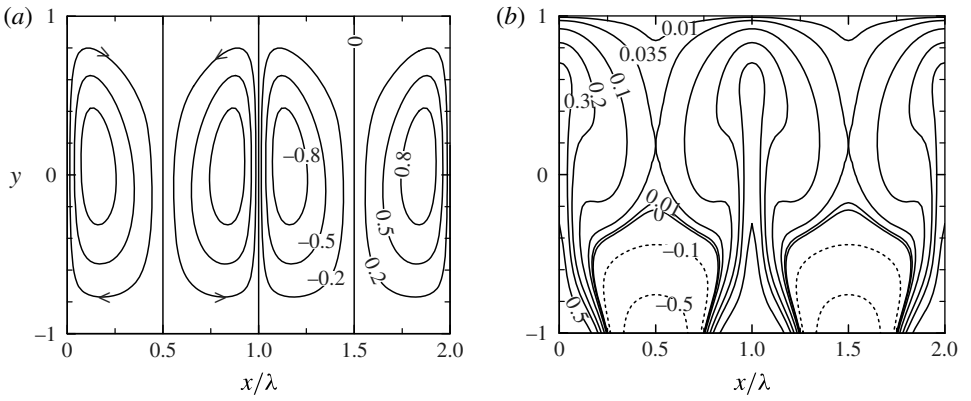


FIGURE 2. Flow topology of type 1. Flow and temperature patterns for the heating intensity $Ra_p = 3500$ and the heating wavenumber $\alpha = 1$ in the absence of the external flow ($Re = 0$). The complete stream function $\Psi(x, y) = Re(-y^3/3 + y + 2/3) + \psi(x, y)$ (*a*) and the complete temperature $\theta(x, y) = Pr^{-1}\theta_0(x, y) + \theta_1(x, y)$ (*b*) are normalized with their maxima where $\psi_{max} = 12.78$ and $\theta_{max} = (2Pr)^{-1}$.

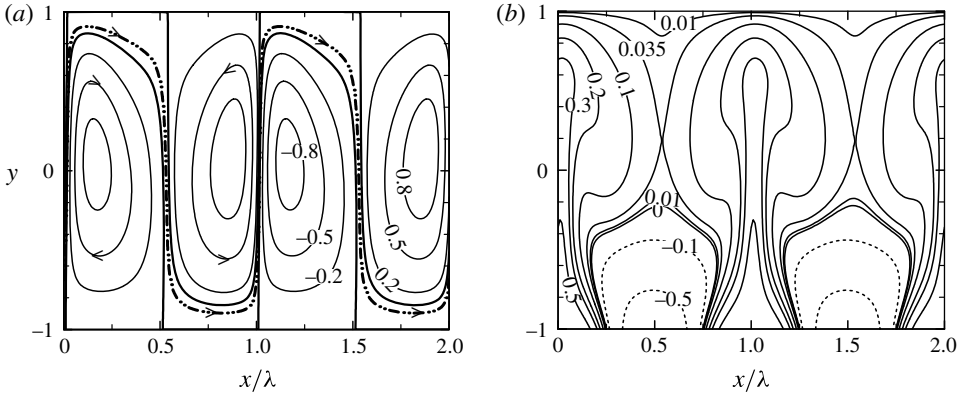


FIGURE 3. Flow topology of type 2. Flow (*a*) and temperature (*b*) patterns for $Re = 1$. $\psi_{max} = 13.34$. Other conditions as in figure 2. The dash–dot line identifies centre of the flow tube.

illustrates the formation of vertical plumes of heated fluid above the hot spots with cooled fluid confined to small regions above the cold spots. Introduction of a weak flow ($Re = 1$) results in the formation of a continuous streamtube directed from left to right which converts rolls into distinct separation bubbles (see figure 3*a*). The streamtube follows an upward direction above the hot spots and a downward direction above the cold spots and, as a result, rolls that were on the right-hand side of the hot spots morph into bubbles attached to the lower wall while rolls from the left-hand side morph into bubbles attached to the upper wall. This flow pattern with separation bubbles at the lower and upper walls is referred to as the type 2 topology. The associated temperature field illustrated in figure 3(*b*) is nearly identical to that found when $Re = 0$ (compare figures 2*b* and 3*b*). Increase of the strength of the horizontal flow to $Re = 10$ increases the size of the streamtube and decreases

https://doi.org/10.1017/jfm.2012.465 Published online by Cambridge University Press

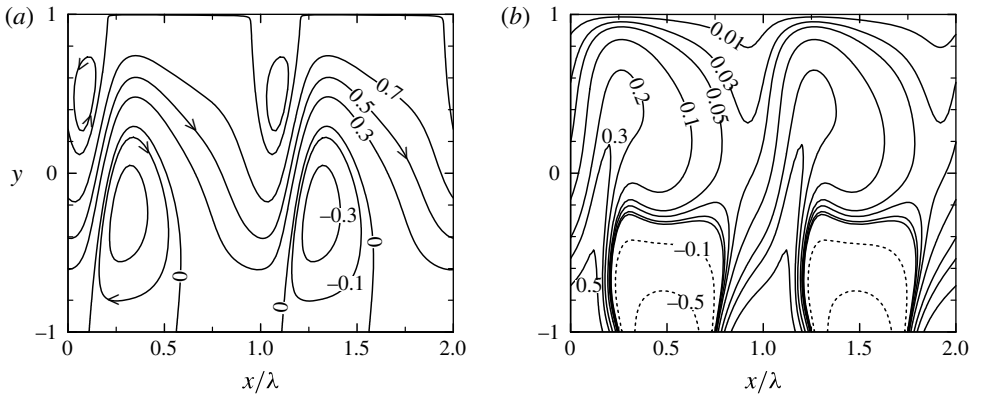


FIGURE 4. Flow (*a*) and temperature (*b*) patterns for $Re = 10$. $\psi_{max} = 14.887$. Other conditions as in figure 2. The resulting flow topology is of type 2.

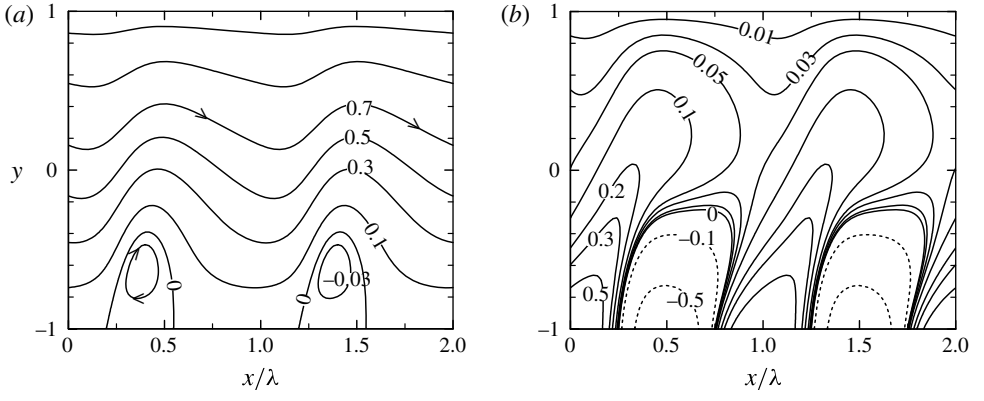


FIGURE 5. Flow topology of type 3. Flow (*a*) and temperature (*b*) patterns for $Re = 20$. $\psi_{max} = 26.667$. Other conditions as in figure 2.

the size of the separation bubbles (figure 4*a*). The thermal plumes become tilted in the streamwise direction while the magnitude of temperature variations remains very similar to that found for smaller *Re* (figure 4*b*). Further increase of the flow strength to $Re = 20$ results in the upper separation bubbles being washed away (figure 5*a*) leading to the type 3 topology. The tilting of the plumes in the streamwise direction is more pronounced and the fluid cools down in the upper section of the channel (figure 5*b*). Increase of the flow strength to $Re = 100$ washes away all separation bubbles (figure 6*a*) resulting in the type 4 topology. Plumes are strongly tilted in the streamwise direction and meaningful changes of the temperature are confined to a thin layer along the lower wall (figure 6*b*). Two additional topologies may appear but only in the case of intense and fairly short-wavelength heating. Figure 7(*a*) illustrates topology of type 5 which includes separation bubbles at the lower wall as well as in-flow bubbles of trapped fluid which split the stream into two sections, one moving above the in-flow bubbles and one below. Topology of type 6 (figure 8*a*) consists of separation bubbles at both walls as well as in-flow bubbles. In both cases fluid trapped

https://doi.org/10.1017/jfm.2012.465 Published online by Cambridge University Press

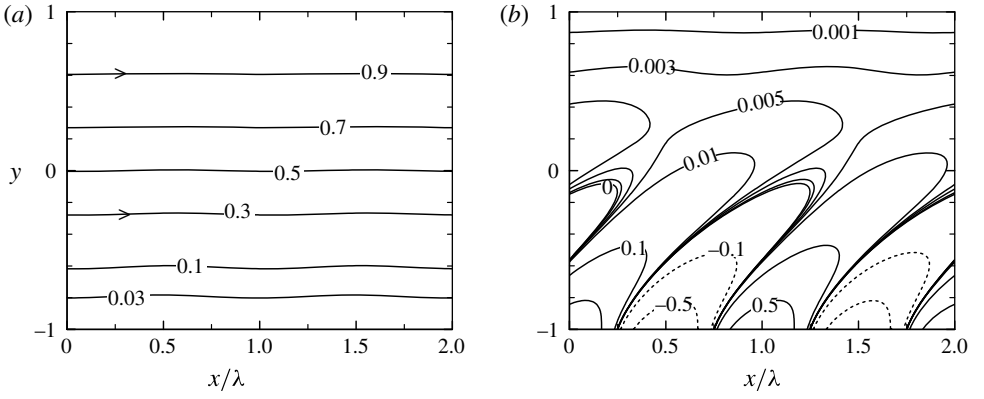


FIGURE 6. Flow topology of type 4. Flow (a) and temperature (b) patterns for $Re = 100$. $\psi_{max} = 133.33$. Other conditions as in figure 2.

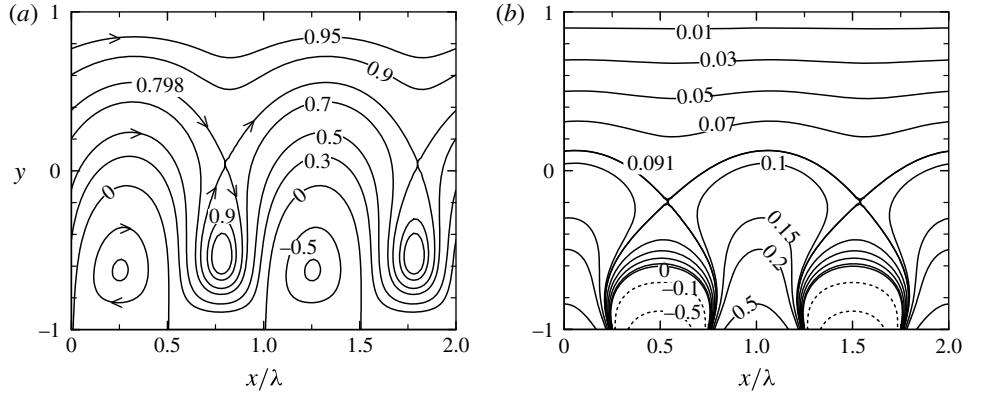


FIGURE 7. Flow topology of type 5. Flow (a) and temperature (b) patterns for $Re = 1$, $\alpha = 5$, $Ra_p = 3500$. $\psi_{max} = 1.365$. Other conditions as in figure 2.

in the in-flow bubbles is almost isothermal and temperature variations in the upper section of the channel are marginal (see figures 7b and 8b).

Conditions leading to the appearance of various topologies are illustrated in figure 9 for $Re = 1$. Type 4 prevails for weak heating. Increase of Ra_p leads to formation of type 3 with the short-wavelength heating requiring higher Ra_p compared with the long-wavelength heating. Type 2 requires still more intense heating and can be generated only by the long-wavelength heating with $\alpha < \sim 4$ in the range of Ra_p considered. Types 5 and 6 require heating that is almost two orders of magnitude higher than type 3 and can only be generated by the short-wavelength heating. Figure 10 illustrates how heating has to be changed as Re increases. In the case of type 3 topology an increase of the Reynolds number from $Re = 1$ to $Re = 50$ increases the required heating by almost three orders of magnitude from $Ra_p = \sim 5$ to $Ra_p = \sim 6000$ over the whole range of α (see figure 10a). Type 2 is more substantially affected by an increase of Re (see figure 10b); the heating wavelengths that can produce this topology and the required heating intensity both increase, e.g. at $Re = 0.01$ this topology can be

https://doi.org/10.1017/jfm.2012.465 Published online by Cambridge University Press

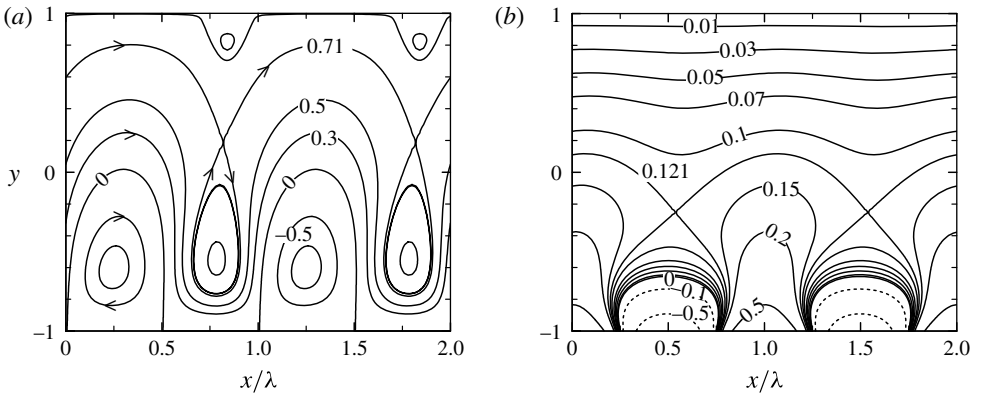


FIGURE 8. Flow topology of type 6. Flow (*a*) and temperature (*b*) patterns for $Re = 1$, $\alpha = 5$, $Ra_p = 5000$. $\psi_{max} = 1.772$. Other conditions as in figure 2.

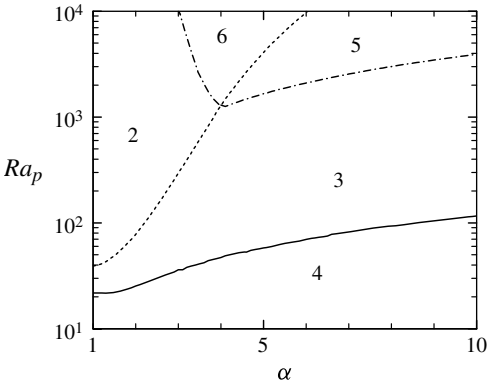


FIGURE 9. Rayleigh number and heating pattern conditions required for the formation of various flow topologies for flow with the Reynolds number $Re = 1$.

generated by $Ra_p = \sim 1$ at $\alpha = 2$, but at $Re = 10$ one needs $Ra_p = \sim 3000$ at the same α.

The variation of the separation bubbles with Ra_p and Re can be utilized in developing various flow control strategies. Mass flow rate can be controlled by increasing/decreasing the heating level while keeping the overall pressure drop the same. A fraction of the fluid volume can be trapped inside separation bubbles for a specified length of time and then removed from the channel by increasing Re; slowing down the flow would re-create bubbles but with different fluid elements trapped inside. The combination of heating and flow strength provides a tool for the management of chemical reactions in micro-vessels, e.g. polymerase chain reaction amplification of DNA (Krishnan, Ugaz & Burns 2002). The effectiveness of the process can be increased by combining heating with appropriate surface topography.

5. Pressure losses

Pressure losses in the unheated channel are described by (2.2). Heating creates various forms and sizes of separation bubbles and thus changes the magnitude and

https://doi.org/10.1017/jfm.2012.465 Published online by Cambridge University Press

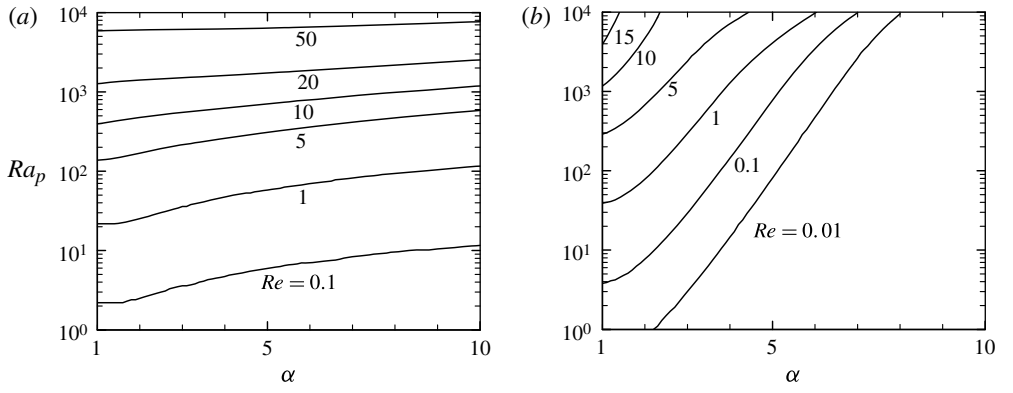


FIGURE 10. Conditions required for the formation of topologies of type 3 (*a*) and type 2 (*b*). Separation bubbles form for the Rayleigh number Ra_p above each of the lines.

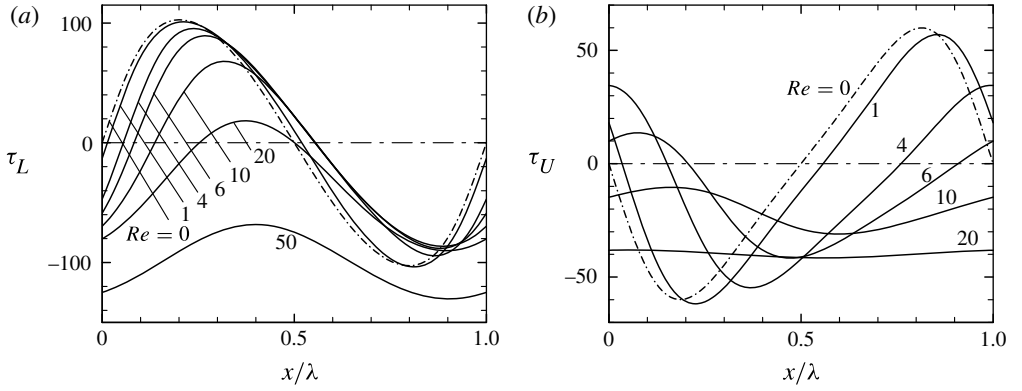


FIGURE 11. Shear stress distribution at the lower (*a*) and upper (*b*) walls for the heating wavenumber $\alpha = 2$ and the Rayleigh number $Ra_p = 2000$.

distribution of the wall shear stress. The distribution of stress acting on the fluid is illustrated in figure 11. For low values of Re the direction of the shear alternates at the two walls, reducing the net drag when compared with the unheated channel. Increasing Re reduces size of the separation bubbles and eventually washes them away, eliminating the drag reducing effect. Increasing the heating intensity extends the range of Re where the drag reduction can be realized.

The total effect is captured by the pressure-gradient correction A defined in (3.3*e*). The complete mean streamwise pressure gradient can be expressed on the basis of (2.2)–(2.3) as

$$\left.\frac{\partial p_2}{\partial x}\right|_{mean} = Re(-2 + A/Re), \tag{5.1}$$

and variations of A/Re are illustrated in figure 12. A significant reduction of pressure loss is realized for small values of Re (flow topology of type 2, see figures 3 and 4). The drag reduction is remarkable when one takes into account the contorted path

https://doi.org/10.1017/jfm.2012.465 Published online by Cambridge University Press

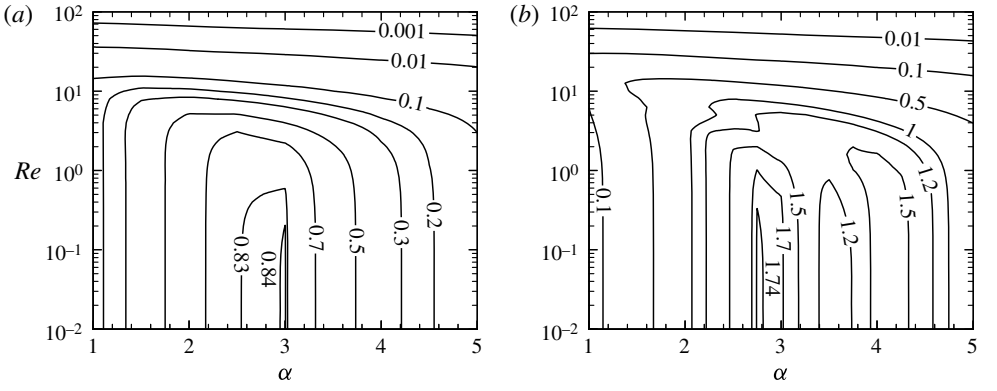


FIGURE 12. Variation of the pressure-gradient correction A/Re as a function of the heating wavenumber α and the flow Reynolds number Re for the heating intensities $Ra_p = 2000$ (*a*) and 5000 (*b*).

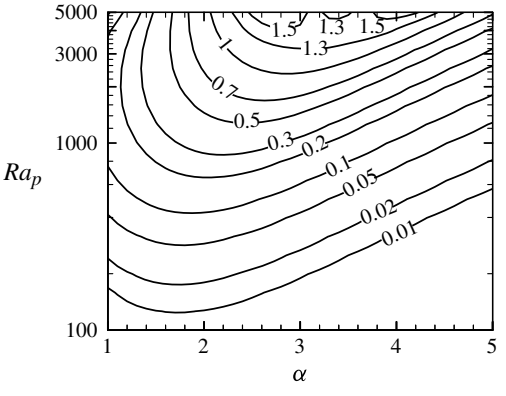


FIGURE 13. Variation of the pressure-gradient correction A/Re as a function of the heating wavenumber α and the Rayleigh number for the flow Reynolds number $Re = 1$.

followed by fluid elements, with a significant increase in the mean length of the path, a significant reduction of the cross-sectional flow area and an increase of the maximum of the x-velocity component above that found in the unheated case (see figures 3 and 4). One should note, however, that motion in the separation bubbles is partially driven by buoyancy which reduces the pressure gradient required to maintain the axial flow.

The drag reduction strongly depends on the heating wavenumber as well as on the heating intensity, with the maximum of $A/Re \approx 0.84$ (42 % drag reduction) occurring for $\alpha \approx 3$ with $Ra_p = 2000$ and $A/Re \approx 1.74$ (87 % drag reduction) for $Ra_p = 5000$. Figure 13 explicitly relates the drag reduction and the heating intensity. The most effective heating pattern changes from $\alpha \approx 1.6$ for $Ra_p \approx 150$ to $\alpha \approx 3$ for $Ra_p = 2500$ while the flow topology changes from type 4 through type 3 to type 2. The drag reduction initially increases proportionally to Ra_p^2 until a saturation is reached, as shown in figure 14. The saturation is due to the formation of the in-flow bubbles,

https://doi.org/10.1017/jfm.2012.465 Published online by Cambridge University Press

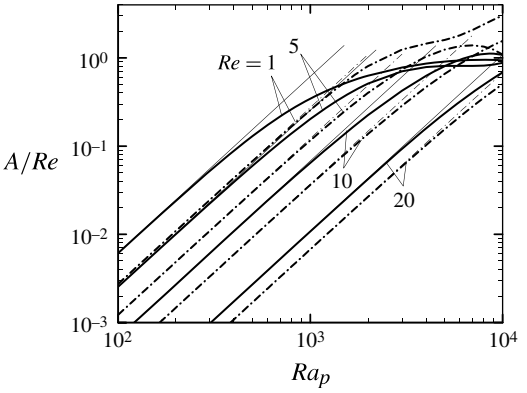


FIGURE 14. Variation of the pressure-gradient correction A/Re as a function of the Rayleigh number Ra_p for the heating wavenumbers $\alpha = 2$ (solid lines) and $\alpha = 3$ (dash–dot lines) and the flow Reynolds number $Re = 1, 5, 10, 20$. Thin lines illustrate results obtained with the weak convection assumption (see § 6).

e.g. topologies of type 5 and 6, which increase viscous dissipation and limit the drag-reducing effect. Saturation effects are also visible in figure 12(*b*) for $Ra_p = 5000$.

6. Mechanics of drag reduction

It has been pointed above that the drag reduction can be explained in terms of the reduced shear acting on the fluid at the walls, and that separation bubbles act like 'rollers' partially propelled by the buoyancy force. We shall now look into the mechanics of drag reduction and focus attention on weak convection. It is convenient to introduce parameter ε as a measure of strength of convection. The explicit identification of ε can be done *a posteriori*. It is sufficient for purposes of this analysis to assume that $\varepsilon \ll 1$, and to represent all flow quantities as asymptotic expansions in powers of ε, i.e.

$$(u_1, v_1, p_1, \theta_1) = \varepsilon(U_1, V_1, P_1, \Theta_1) + \varepsilon^2 (U_2, V_2, P_2, \Theta_2) + O(\varepsilon^3). \tag{6.1}$$

Substitution of (6.1) into (2.5) and retention of terms of the two highest orders of magnitude lead to a system of $O(\varepsilon)$ in the form

$$\nabla^2 U_1 - Re\, u_0 \frac{\partial U_1}{\partial x} - Re\, V_1 \frac{\mathrm{d}u_0}{\mathrm{d}y} - \frac{\partial P_1}{\partial x} = 0, \tag{6.2a}$$

$$\nabla^2 V_1 - Re\, u_0 \frac{\partial V_1}{\partial x} - \frac{\partial P_1}{\partial y} = -Ra_p\, \Theta_1 - Ra_p\, Pr^{-1} \hat{\theta}_0, \tag{6.2b}$$

$$\nabla^2 \Theta_1 - PrRe\, u_0 \frac{\partial \Theta_1}{\partial x} = Re\, u_0 \frac{\partial \hat{\theta}_0}{\partial x}, \tag{6.2c}$$

$$\frac{\partial U_1}{\partial x} + \frac{\partial V_1}{\partial y} = 0, \tag{6.2d}$$

where $\hat{\theta}_0 = \theta_0/\varepsilon = O(1)$, and a system of $O(\varepsilon^2)$ of the form

$$\nabla^2 U_2 - Re\, u_0 \frac{\partial U_2}{\partial x} - Re\, V_2 \frac{\mathrm{d}u_0}{\mathrm{d}y} - \frac{\partial P_2}{\partial x} = U_1 \frac{\partial U_1}{\partial x} + V_1 \frac{\partial U_1}{\partial y}, \tag{6.3a}$$

https://doi.org/10.1017/jfm.2012.465 Published online by Cambridge University Press

$$\nabla^2 V_2 - Re\, u_0 \frac{\partial V_2}{\partial x} - \frac{\partial P_2}{\partial y} = -Ra_p\, \Theta_2 + U_1 \frac{\partial V_1}{\partial x} + V_1 \frac{\partial V_1}{\partial y}, \tag{6.3b}$$

$$\nabla^2 \Theta_2 - Pr\, Re\, u_0 \frac{\partial \Theta_2}{\partial x} = U_1 \frac{\partial \hat{\theta}_0}{\partial x} + V_1 \frac{\partial \hat{\theta}_0}{\partial y} + Pr\, U_1 \frac{\partial \Theta_1}{\partial x} + Pr\, V_1 \frac{\partial \Theta_1}{\partial y}, \tag{6.3c}$$

$$\frac{\partial U_2}{\partial x} + \frac{\partial V_2}{\partial y} = 0. \tag{6.3d}$$

Both systems are supplemented by the homogeneous boundary conditions and constraints associated with the fixed-flow-rate condition.

Since ε is undefined at this stage, (6.2) is rearranged as

$$\nabla^2 \tilde{\Theta}_1 - PrRe\, u_0 \frac{\partial \tilde{\Theta}_1}{\partial x} = Re\, u_0 \frac{\partial \theta_0}{\partial x}, \tag{6.4}$$

where $\tilde{\Theta}_1 = \varepsilon \Theta_1$. Forcing on the right-hand side of (6.4) is given by (2.4) and leads to a solution of the form

$$\tilde{\Theta}_1(x, y) = \tilde{\Theta}_1^{(1)}(y) \mathrm{e}^{\mathrm{i}\alpha x} + \text{c.c.} \tag{6.5}$$

where c.c. stands for the complex conjugate and $\tilde{\Theta}_1^{(1)}$ comes from solution of the following problem:

$$\mathrm{D}^2 \tilde{\Theta}_1^{(1)} - (\alpha^2 + \mathrm{i}\,\alpha\, Pr\, Re\, u_0)\, \tilde{\Theta}_1^{(1)} = \mathrm{i}\,\alpha\, Re\, u_0\, \theta_0^{(1)}, \quad \tilde{\Theta}_1^{(1)}(\pm 1) = 0. \tag{6.6}$$

The flow problem at the leading order of approximation is described by (6.2*a*,*b*,*d*). Introduction of the stream function and elimination of the pressure result in a single equation in the form

$$\mathrm{D}^4 \psi - Re\, u_0 \left(\frac{\partial^3 \psi}{\partial x \partial y^2} + \frac{\partial^3 \psi}{\partial x^3} \right) + Re\, \mathrm{D}^2 u_0 \frac{\partial \psi}{\partial x} = Ra_p \frac{\partial \Theta_1}{\partial x} + Ra_p\, Pr^{-1} \frac{\partial \hat{\theta}_0}{\partial x}. \tag{6.7}$$

The type of forcing on the right-hand side suggests a solution of the form

$$\varepsilon \psi(x, y) = \tilde{\psi}(x, y) = \tilde{\varphi}^{(1)}(y) \mathrm{e}^{\mathrm{i}\alpha x} + \text{c.c.} \tag{6.8}$$

Substitution of (2.4), (6.5) and (6.8) into (6.7) leads to

$$\begin{aligned} &\mathrm{D}^4 \tilde{\varphi}^{(1)} - (2\alpha^2 + \mathrm{i}\alpha\, Re\, u_0)\, \mathrm{D}^2 \tilde{\varphi}^{(1)} + (\alpha^4 + \mathrm{i}\alpha^3 Re\, u_0 + \mathrm{i}\alpha\, Re\, \mathrm{D}^2 u_0)\, \tilde{\varphi}^{(1)} \\ &\quad = \mathrm{i}\alpha\, Ra_p\, \tilde{\Theta}_1^{(1)} + \mathrm{i}\alpha\, Ra_p Pr^{-1} \theta_0^{(1)}, \end{aligned} \tag{6.9a}$$

$$\tilde{\varphi}^{(1)}(\pm 1) = \mathrm{D}\tilde{\varphi}^{(1)}(\pm 1) = 0, \tag{6.9b}$$

whose solution describes the modal function $\tilde{\varphi}^{(1)}$. The velocity components have the form

$$\varepsilon U_1 = \tilde{U}_1 = \varepsilon\, \partial\psi/\partial y = \partial\tilde{\psi}/\partial y = \mathrm{D}\tilde{\varphi}^{(1)}(y)\, \mathrm{e}^{\mathrm{i}\alpha x} + \text{c.c.} = \tilde{U}_1^{(1)}(y) \mathrm{e}^{\mathrm{i}\alpha x} + \text{c.c.}, \tag{6.10a}$$

$$\varepsilon V_1 = \tilde{V}_1 = \varepsilon\, \partial\psi/\partial x = \partial\tilde{\psi}/\partial x = \mathrm{i}\alpha\, \tilde{\varphi}^{(1)}(y)\, \mathrm{e}^{\mathrm{i}\alpha x} + \text{c.c.} = \tilde{V}_1^{(1)}(y) \mathrm{e}^{\mathrm{i}\alpha x} + \text{c.c.} \tag{6.10b}$$

Analysis of the next order of approximation for temperature starts with (6.3*c*) multiplied by ε and followed by substitution of (2.4), (6.5) and (6.10). Forcing on the right-hand side of (6.3*c*) contains terms proportional to e^0 and $\mathrm{e}^{2\mathrm{i}\alpha x}$ which leads to a solution of the form

$$\tilde{\Theta}_2(x, y) = \tilde{\Theta}_2^{(0)} + (\tilde{\Theta}_2^{(2)}(y) \mathrm{e}^{2\mathrm{i}\alpha x} + \text{c.c.}) \tag{6.11}$$

https://doi.org/10.1017/jfm.2012.465 Published online by Cambridge University Press

and demonstrates the appearance of a net heat transfer between the two walls. Details are not given due to the length of the equations.

Analysis of the next order of approximation for the flow field starts with (6.3*a,b,d*) multiplied by ε and followed by substitution of (2.4), (6.5), (6.10) and (6.11). Forcing on the right-hand side of (6.3*a,b*) contains terms proportional to e^0 and $\mathrm{e}^{2\mathrm{i}\alpha x}$ which leads to a solution of the form

$$\varepsilon U_2(x,y) = \tilde{U}_2(x,y) = \tilde{U}_2^{(0)} + (\tilde{U}_2^{(2)}(y)\mathrm{e}^{2\mathrm{i}\alpha x} + \text{c.c.}), \tag{6.12a}$$

$$\varepsilon V_2(x,y) = \tilde{V}_2(x,y) = \tilde{V}_2^{(0)} + (\tilde{V}_2^{(2)}(y)\mathrm{e}^{2\mathrm{i}\alpha x} + \text{c.c.}), \tag{6.12b}$$

$$\varepsilon P_2(x,y) = \tilde{P}_2(x,y) = \tilde{P}_2^{(0)} + \tilde{A}x + (\tilde{P}_2^{(2)}(y)\mathrm{e}^{2\mathrm{i}\alpha x} + \text{c.c.}). \tag{6.12c}$$

It is simple to show that $\tilde{V}_2^{(0)} = 0$. Substitution of (6.10) and (6.12) into (6.3*a*) and extraction of mode zero leads to the following problem:

$$\mathrm{D}^2\tilde{U}_2^{(0)} = V_1^{(1)}\mathrm{D}\tilde{U}_1^{(-1)} + V_1^{(-1)}\mathrm{D}\tilde{U}_1^{(1)} + \tilde{A}, \quad \tilde{U}_2^{(0)}(\pm 1) = 0, \quad \int_{-1}^{1}\tilde{U}_2^{(0)}\,\mathrm{d}y = 0 \tag{6.13a–c}$$

where (6.13*c*) represents the flow-rate constraint. The pressure-gradient correction can be evaluated as

$$A = 1.5(K_1 - K_2) \tag{6.14a}$$

where

$$K_1 = \int_{-1}^{1} f(y)\,\mathrm{d}y, \quad K_2 = f(1), \quad f(y) = \int_{-1}^{y} g(y)\,\mathrm{d}y, \quad g(y) = \tilde{V}_1^{(1)}\tilde{U}_1^{(-1)} + \tilde{V}_1^{(-1)}\tilde{U}_1^{(1)} \tag{6.14b–e}$$

without the need for an explicit determination of ε. In the above, $\tilde{A} = \varepsilon A$. Equation (6.14) demonstrates that the pressure-gradient correction results from the nonlinear effects associated with the buoyancy-induced motion. Equation (6.14*b*) represents the Reynolds stress integrated over one wavelength in the x-direction, and K_2, (6.14*c*), represents this stress integrated across the channel. It may be concluded that the pressure-gradient-reducing effect is a result of the Reynolds stress created by the heating. In the following discussion we shall refer to $g(y)$ as the Reynolds stress function. A general solution of (6.6), (6.9) and (6.14) has been determined using the same collocation method as described in § 3. Integrations in (6.14) have been carried out with fourth-order accuracy.

We shall now discuss in detail how the Reynolds stress changes as a function of the intensity of the axial flow (Re), the intensity of the heating (Ra_p) and the pattern of heating (α). We begin the discussion with the effects of Re. When $Re = 0$, solution of (6.6) is trivial, i.e. $\tilde{\Theta}_1 = 0$, convective motion is described by (6.9), the resulting $\tilde{U}_1$ is purely imaginary and $\tilde{V}_1$ is purely real, the phase shift between $\tilde{U}_1$ and $\tilde{V}_1$ is $\pi/2$, the Reynolds stress function $g(y)$ becomes null and the pressure-gradient correction becomes zero. Convection is purely periodic in x, and it does not contribute to nor generate any net axial motion. The form of (6.14*b*) demonstrates that the phase shift has to be different from $\pi/2$ in order to generate a non-zero A.

Assume now that Re is small but finite. The solution for (6.6) and (6.9) can be represented as asymptotic expansions in terms of Re of the form:

$$\left.\begin{aligned} &\Theta_r = Re\,\Theta_{r1} + Re^2\Theta_{r2} + O(Re^3), \quad \Theta_i = Re\,\Theta_{\mathrm{i}1} + Re^2\Theta_{\mathrm{i}2} + O(Re^3), \\ &\tilde{\Theta}_1^{(1)} = \Theta_r + \mathrm{i}\Theta_i, \end{aligned}\right\} \tag{6.15a}$$

https://doi.org/10.1017/jfm.2012.465 Published online by Cambridge University Press

$$\varphi_r = \varphi_{r0} + Re\,\varphi_{r1} + O(Re^2), \quad \varphi_i = \varphi_{i0} + Re\,\varphi_{i1} + O(Re^2), \quad \tilde{\varphi}_1^{(1)} = \varphi_r + \mathrm{i}\varphi_i. \quad (6.15b)$$

Substitution of (6.15) into (6.6) and retention of terms proportional to the two lowest powers of Re results in the following systems:

$$O(Re): \quad \mathrm{D}^2\Theta_{r1} - \alpha^2\,\Theta_{r1} = 0, \quad \mathrm{D}^2\Theta_{i1} - \alpha^2\,\Theta_{i1} = \alpha\,u_0\theta_0^{(1)}, \quad (6.16a\text{–}b)$$

$$O(Re^2): \quad \mathrm{D}^2\Theta_{r2} - \alpha^2\,\Theta_{r2} = -\alpha\,Pr\,u_0\Theta_{i1}, \quad \mathrm{D}^2\Theta_{i2} - \alpha^2\,\Theta_{i2} = 0. \quad (6.17a\text{–}b)$$

It is obvious that $\Theta_{r1} = 0$ and $\Theta_{i2} = 0$, and (6.17*a*) has been simplified accordingly. The same process applied to (6.9) result in the systems:

$$O(Re^0): \quad \mathrm{D}^4\varphi_{r0} - 2\alpha^2\mathrm{D}^2\varphi_{r0} + \alpha^4\varphi_{r0} = 0, \quad (6.18a)$$

$$\mathrm{D}^4\varphi_{i0} - 2\alpha^2\mathrm{D}^2\varphi_{i0} + \alpha^4\varphi_{i0} = \alpha\,Ra\,Pr^{-1}\theta_0^{(1)}, \quad (6.18b)$$

$$O(Re^1): \quad \mathrm{D}^4\varphi_{r1} - 2\alpha^2\mathrm{D}^2\varphi_{r1} + \alpha^4\varphi_{r1} = -\alpha\,u_0\,\mathrm{D}^2\varphi_{i0} + (\alpha^3\,u_0 + \alpha\,\mathrm{D}^2u_0)\,\varphi_{i0}, \quad (6.19a)$$

$$\mathrm{D}^4\varphi_{i1} - 2\alpha^2\mathrm{D}^2\varphi_{i1} + \alpha^4\varphi_{i1} = 0. \quad (6.19b)$$

It is again simple to show that $\varphi_{r0} = 0$ and $\varphi_{i1} = 0$, and (6.19*a*) has been simplified accordingly. Explicit evaluations of Θ_{i1}, Θ_{r2}, φ_{i0} and φ_{r1}, which require numerical work, are not required for the further discussion. The forms of the velocity components associated with convection, i.e. $\tilde{U}_1^{(1)} = \lfloor Re\,\mathrm{D}\varphi_{r1} + O(Re^3)\rfloor + \mathrm{i}\lfloor \mathrm{D}\varphi_{i0} + O(Re^2)\rfloor$ and $\tilde{V}_1^{(1)} = \lfloor \alpha\,\varphi_{i0} + O(Re^2)\rfloor + \mathrm{i}\lfloor -\alpha\,Re\,\varphi_{r1} + O(Re^3)\rfloor$, explicitly demonstrate that the axial flow is responsible for change in the phase difference between $\tilde{U}_1^{(1)}$ and $\tilde{V}_1^{(1)}$ leading to formation of the non-zero Reynolds stress function. The form of this function, i.e.

$$g(y) = 2\,Re\,\alpha\,\varphi_{i0}\,\mathrm{D}\varphi_{r1} + O\,(Re^2), \quad (6.20)$$

demonstrates that the pressure-gradient correction increases proportionally to Re. This prediction is confirmed by solution of the complete flow problem displayed in figure 12 (see also figure 17).

Variations of the pressure-gradient correction for large Re are more complex but can be explained in qualitative terms, nevertheless. Equation (6.6) describing the temperature field has a variable coefficient containing the product (Re u_0) and an inhomogeneous term with a similar product. When $Re \to \infty$, these products are large everywhere except close to the walls where $u_0 \approx 0$ and thus wall (transition) layers may form. It can be shown that the solution has the form

$$\Theta_r \approx -Pr^{-1}\theta_0^{(1)}, \quad \Theta_i \approx 0 \quad (6.21)$$

everywhere except near the bottom wall where $\theta_0^{(1)} \neq 0$. The formation of wall layer for a few values of Re is illustrated in figure 15; the decrease of its thickness with an increase of Re is clearly visible. Substitution of (6.21) into (2.4) shows that the flow becomes nearly isothermal outside the wall layer and thus the heating effect (and the buoyancy force) are confined to this layer only. This fact is also illustrated in figure 6(*b*) displaying isotherms of the complete temperature field.

Equation (6.9) describing the velocity field contains a variety of coefficients, including some that are similar to those found in (6.6). Detailed analysis is cumbersome but the qualitative character of the solution for large Re can be deduced by looking at the forcing terms on the right-hand side. This forcing disappears outside the heated wall layer as illustrated explicitly in figure 16 (see also (6.21)). The driving force (buoyancy) is confined to a thin wall layer but the resulting motion spreads into the complete flow domain where it is opposed by friction. An increase of Re

https://doi.org/10.1017/jfm.2012.465 Published online by Cambridge University Press

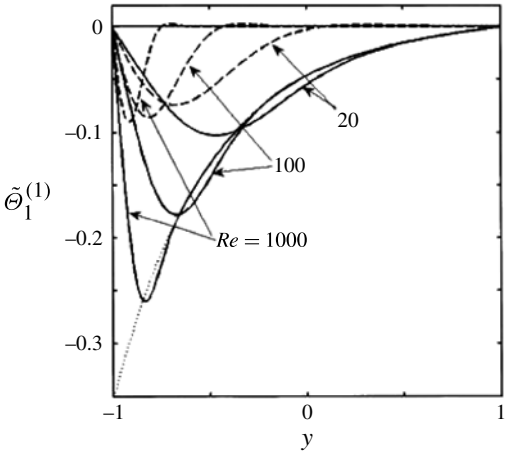


FIGURE 15. Distribution of the temperature modal function $\tilde{\Theta}_1^{(1)}$ for the heating wavenumber $\alpha = 2$ and the Rayleigh number $Ra_p = 200$ for the flow Reynolds numbers $Re = 20, 100, 1000$. Solid and dashed lines correspond to the real and imaginary parts of $\tilde{\Theta}_1^{(1)}$, respectively. Dotted line illustrates conduction effect $(-Pr^{-1}\theta_0^{(1)})$.

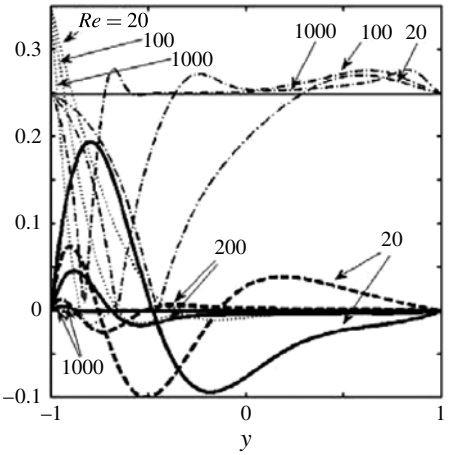


FIGURE 16. Distribution of the $\tilde{U}_1^{(1)}$ modal function for the flow Reynolds numbers $Re = 20, 100, 1000$ and convection corresponding to the Rayleigh number $Ra_p = 200$ and the heating wavenumber $\alpha = 2$. Solid and dashed lines correspond to the real and imaginary parts, respectively. Dotted lines illustrate distribution of the forcing function $(\mathrm{i}\alpha\, Ra_p\, \tilde{\Theta}_1^{(1)} + \mathrm{i}\alpha\, Ra_p Pr^{-1}\theta_0^{(1)})$ appearing on the right-hand side of (6.9*a*) for the same values of Re, and the dash–dot lines show distribution of $\delta/2\pi$ where δ is the phase difference between $\tilde{U}_1^{(1)}$ and $\tilde{V}_1^{(1)}$.

reduces the thickness of the wall layer, reduces the effectiveness of the driving force and results in a less intense motion concentrated closer and closer to the lower wall, as illustrated in figure 16. The pressure-gradient correction decreases as a result of the weaker convection. An additional decrease results from the rearrangement of the phase difference between $\tilde{U}_1$ and $\tilde{V}_1$, as illustrated in figure 16. This phase difference

https://doi.org/10.1017/jfm.2012.465 Published online by Cambridge University Press

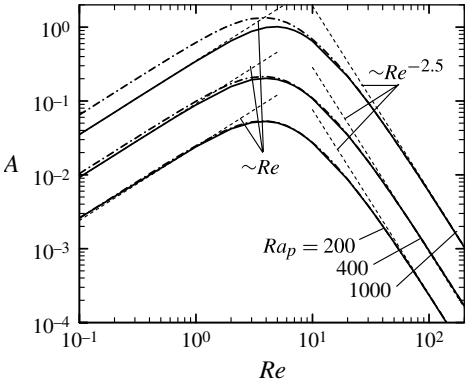


FIGURE 17. Variation of the pressure-gradient correction A as a function of the flow Reynolds number Re for the heating corresponding to the Rayleigh numbers $Ra_p = 200, 400, 1000$ and the wavenumber $\alpha = 2$. Solid and dash–dot lines correspond to solutions of the complete and simplified (see § 6) problems, respectively. Dashed lines identify asymptotes.

is nearly $\pi/2$ outside the wall layer, rapidly changes across this layer and returns back to $\pi/2$ as $y \to -1$.

The variation of the pressure-gradient correction as a function of Re for the whole range of Re of practical interest is illustrated in figure 17. Correction A increases linearly for small Re, reaches a certain maximum and then rapidly drops off when Re becomes large. The same pattern can also be observed in figure 12.

Consider now the effects of the heating intensity. An increase of the Rayleigh number Ra_p is expected to increase the pressure-gradient correction. Since both $\tilde{U}_1^{(1)}$ and $\tilde{V}_1^{(1)}$ are directly proportional to Ra_p, this increase is proportional to Ra_p^2, as illustrated in figure 14. This figure also demonstrates that the simplified analysis presented in this section is valid for surprisingly large Ra_p values. If convection is too strong, secondary structures appear resulting in the reduction of A, as has already been discussed in § 5 (see figures 13 and 14).

The pattern of heating, as quantified by the heating wavenumber α, also has a strong effect on the form of convection and thus on the Reynolds stress. The analysis begins with long-wavelength heating, i.e. $\alpha \to 0$. Forcing expressed by (2.4) can be approximated as

$$\theta_0^{(1)} = (1+y)/8 + \alpha^2\,(y^2-1)/16 + O(\alpha^4) \tag{6.22}$$

and this permits representation of the solution in the form of asymptotic expansions in power of α, i.e.

$$\tilde{\Theta}_1^{(1)} = \alpha\, G_1 + \alpha^2 G_2 + O(\alpha^3), \quad \tilde{\varphi}_1^{(1)} = \alpha\, F_1 + \alpha^2 F_2 + O(\alpha^3). \tag{6.23}$$

Substitution of (6.22)–(6.23) into (6.6) and (6.9) and retention of terms of the two lowest powers in α results in the following systems:

$$O(\alpha): \quad \mathrm{D}^2 G_1 = \mathrm{i}\,Re\,u_0(1-y)/8, \quad \mathrm{D}^2 G_2 = \mathrm{i}\,Re\,Pr\,u_0\,G_1, \tag{6.24}$$

$$\left.\begin{aligned} O(\alpha^2): \quad & \mathrm{D}^4 F_1 = \mathrm{i}\,Ra_p\,Pr^{-1}(1-y)/8, \\ & \mathrm{D}^4 F_2 = \mathrm{i}\,Re\,u_0\,\mathrm{D}^2 F_1 - \mathrm{i}\,Re\,\mathrm{D}^2 u_0\,F_1 + \mathrm{i}\,Ra_p\,G_1, \end{aligned}\right\} \tag{6.25}$$

https://doi.org/10.1017/jfm.2012.465 Published online by Cambridge University Press

supplemented by the homogeneous boundary conditions. Solutions of both systems can be determined explicitly but it is sufficient for the purposes of this discussion to note that G_1 and F_1 are purely imaginary, and G_2 and F_2 are purely real. It is simple to show that the Reynolds stress function $g(y)$ can be expressed as

$$g(y) = 2\alpha^4 \left(\hat{F}_1 \, \mathrm{D}F_2 + F_2 \, \mathrm{D}\hat{F}_1\right) \tag{6.26}$$

where $F_1 = \mathrm{i}\hat{F}_1$, which demonstrates that the pressure-gradient correction decreases proportionally to α^4. Part of this decrease is due to the weakening of the convection for smaller α and part is due to the phase shift between $\tilde{U}_1^{(1)}$ and $\tilde{V}_1^{(1)}$ approaching $\pi/2$. This prediction is confirmed by solution of the complete problem displayed in figure 19.

Analysis of flow response for short-wavelength heating, $\alpha \to \infty$, begins by noting that the thermal forcing can be approximated as

$$\theta_0^{(1)}(y) = 0.25\mathrm{e}^{-\alpha(1+y)}. \tag{6.27}$$

Substitution of (6.27) into (6.6) and introduction of a stretched variable $Y = \alpha(y+1)$ and representation of the velocity u_0 in terms of Y leads to

$$\begin{aligned} &\frac{\mathrm{d}^2\tilde{\Theta}_1^{(1)}}{\mathrm{d}Y^2} - \left[1 + \alpha^{-2}\,\mathrm{i}\,Pr\,Re\,\left(2Y - \alpha^{-1}Y^2\right)\right]\,\tilde{\Theta}_1^{(1)} \\ &\quad = 0.25\,\alpha^{-2}\,\mathrm{i}\,Re\,\left(2Y - \alpha^{-1}Y^2\right)\,\mathrm{e}^{-Y}. \end{aligned} \tag{6.28}$$

A solution of (6.28) is assumed in the form of an asymptotic expansion in powers of α^{-1}, i.e.

$$\tilde{\Theta}_1^{(1)} = \alpha^{-2} H_2 + \alpha^{-3} H_3 + O(\alpha^{-4}). \tag{6.29}$$

Its substitution into (6.28) and retention of the two leading-order terms results in the following systems:

$$O(\alpha^{-2}): \quad \frac{\mathrm{d}^2 H_2}{\mathrm{d}Y^2} - H_2 = 0.5\,\mathrm{i}\,Re\,Y\mathrm{e}^{-Y}, \tag{6.30a}$$

$$O(\alpha^{-3}): \quad \frac{\mathrm{d}^2 H_3}{\mathrm{d}Y^2} - H_3 = -0.25\,\mathrm{i}\,Re\,Y^2\mathrm{e}^{-Y}, \tag{6.30b}$$

supplemented by the homogeneous boundary conditions. The solutions are

$$H_2 = -0.125\,\mathrm{i}\,Re\,(Y + Y^2)\mathrm{e}^{-Y}, \quad H_3 = 0.125\,\mathrm{i}\,Re\,(Y/2 + Y^2/2 + Y^3/3)\mathrm{e}^{-Y}. \tag{6.31a,b}$$

Figure 18 shows that temperature modulations created by convection are not able to penetrate deep into the channel. The thickness of the penetration zone as well as the maximum temperature correction decrease rapidly with an increase of α.

A similar process applied to the flow problem results in a modal equation of the form

$$\begin{aligned} &\frac{\mathrm{d}^4\tilde{\varphi}^{(1)}}{\mathrm{d}Y^4} + \left[-2 + \mathrm{i}\alpha^{-2}Re\,\left(2Y - \alpha^{-1}Y^2\right)\right]\frac{\mathrm{d}^2\tilde{\varphi}^{(1)}}{\mathrm{d}Y^2} \\ &\qquad + \left[1 + \mathrm{i}\alpha^{-2}Re\,\left(2Y - \alpha^{-1}Y^2\right) - 2\,\mathrm{i}\alpha^{-3}Re\right]\tilde{\varphi}^{(1)} \\ &\quad = \mathrm{i}\alpha^{-3}\,Ra\,\left(\alpha^{-2}H_2 + \alpha^{-3}H_3\right) + 0.25\,\mathrm{i}\alpha^{-3}\,Ra_p Pr^{-1}\mathrm{e}^{-Y}. \end{aligned} \tag{6.32}$$

The solution is assumed as an asymptotic expansion

$$\tilde{\varphi}_1^{(1)} = \alpha^{-3} B_3 + \alpha^{-4} B_4 + \alpha^{-5} B_5 + O(\alpha^{-6}). \tag{6.33}$$

https://doi.org/10.1017/jfm.2012.465 Published online by Cambridge University Press

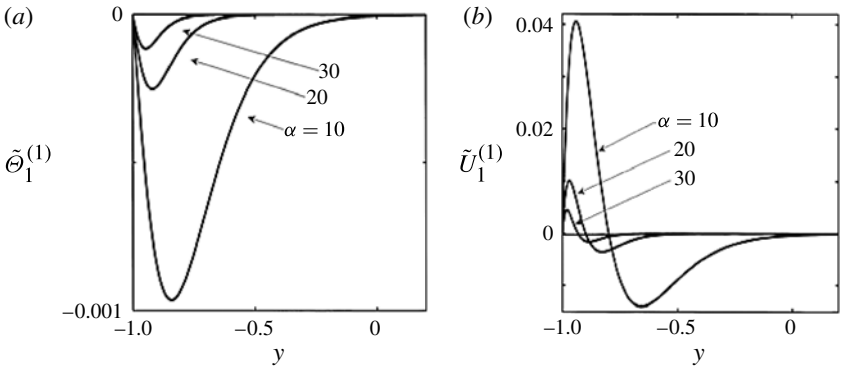


FIGURE 18. Distribution of the imaginary part of the temperature modal function $\tilde{\Theta}_1^{(1)}$ (*a*) and real part of the *u*-velocity modal function $\tilde{U}_1^{(1)}$ (*b*) for the heating wavenumbers $\alpha = 10, 20, 30$ and the heating intensity corresponding to the Rayleigh number $Ra_p = 200$ with the flow corresponding to the Reynolds number $Re = 1$.

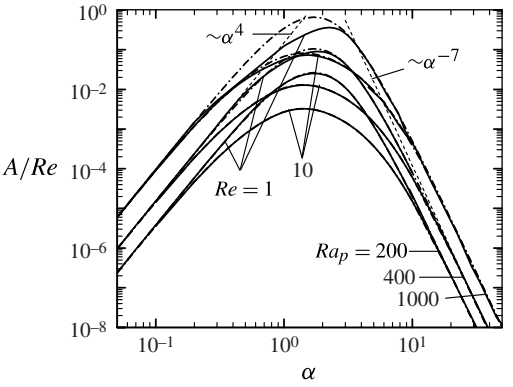


FIGURE 19. Variation of the pressure-gradient correction A/Re as a function of the heating wavenumber α for the flow Reynolds numbers $Re = 1, 10$ and the heating intensity corresponding to the Rayleigh numbers $Ra_p = 200, 400, 1000$. Solid and dash–dot lines correspond to solutions of the complete and simplified (see § 6) problems, respectively. Dashed lines identify asymptotes.

Its substitution into (6.32) and retention of terms of the three leading orders of magnitude results in the following systems:

$$O(\alpha^{-3}): \quad \frac{\mathrm{d}^4 B_3}{\mathrm{d}Y^4} - 2\frac{\mathrm{d}^2 B_3}{\mathrm{d}Y^2} + B_3 = 0.25\,\mathrm{i}\,Ra_p Pr^{-1}\mathrm{e}^{-Y}, \tag{6.34a}$$

$$O(\alpha^{-4}): \quad \frac{\mathrm{d}^4 B_4}{\mathrm{d}Y^4} - 2\frac{\mathrm{d}^2 B_4}{\mathrm{d}Y^2} + B_4 = 0, \tag{6.34b}$$

$$O(\alpha^{-5}): \quad \frac{\mathrm{d}^4 B_5}{\mathrm{d}Y^4} - 2\frac{\mathrm{d}^2 B_5}{\mathrm{d}Y^2} + B_5 = -\mathrm{i}\,Re\,\left(2Y - Y^2\right)\frac{\mathrm{d}^2 B_3}{\mathrm{d}Y^2} - \mathrm{i}\,Re\,\left(2Y - Y^2\right)\,B_3 - \mathrm{i}\,Ra_p H_2. \tag{6.34c}$$

https://doi.org/10.1017/jfm.2012.465 Published online by Cambridge University Press

Solutions have the form

$$B_3 = \mathrm{i}\, Ra_p\, Pr^{-1}\, Y^2 \mathrm{e}^Y/32, \quad B_4 = 0. \tag{6.35a–b}$$

It is sufficient to note that B_5 is purely real. The velocity components have the form

$$\tilde{U}_1^{(1)}(y) = O(\alpha^{-4}) + \mathrm{i}\left[\alpha^{-2} Ra_p\, Pr^{-1}(2Y - Y^2)\mathrm{e}^{-Y}/32 + O(\alpha^{-5})\right], \tag{6.36a}$$

$$\tilde{V}_1^{(1)} = \lfloor \alpha^{-2} Ra_p\, Pr^{-1} Y^2\, \mathrm{e}^{-Y}/32 + O(\alpha^{-5})\rfloor + \mathrm{i}\, O(\alpha^{-4}), \tag{6.36b}$$

which lead to the Reynolds stress function $g(y) = O(\alpha^{-7})$ and the pressure-gradient correction decreasing as α^{-7} when α increases. This prediction is verified by comparison with the solution of the complete problem displayed in figure 19. The decrease is primarily due to the weakening of the convection as the effect of Re, and thus the phase change between $\tilde{U}_1^{(1)}$ and $\tilde{V}_1^{(1)}$, contribute at the level $O(\alpha^{-7})$. Figure 18(*b*) explicitly demonstrates that the depth of convection penetration is very small and that the intensity of convection rapidly decreases as α increases.

Figure 19 illustrates the variation of the pressure-gradient correction over a wide range of heating wavenumbers. It is clear that the magnitude of drag reduction of practical interest can be generated only by heating with the wavenumbers $O(1)$. Both an excessive reduction and an excessive increase of α reduce the intensity of the convection and alter its spatial distribution in such a way that the Reynolds stress function rapidly diminishes resulting in a rapid decrease of the pressure-gradient correction.

7. Summary

The principle of drag reduction due to spatially modulated heating has been described. The drag-reducing effect relies on the formation of separation bubbles. The size, distribution and intensity of motion inside these bubbles are controlled by the pattern and intensity of the externally imposed heating. Two mechanisms contribute to the overall effect. In the first, the bubbles separate the main stream from the bounding walls and, as a result, the walls are in contact with a slowly moving fluid inside separation zones rather than with the main stream and, thus, are exposed to a reduced shear. This mechanism is qualitatively similar to the superhydrophobic effect where bubbles of fluid with viscosity smaller than the main stream separate this stream from the bounding walls. The second mechanism takes advantage of the buoyancy force which contributes to the fluid rotation inside separation bubbles and, in this way, creates a supplementary propulsive force that reduces the magnitude of the pressure gradient required to drive the prescribed mass flow rate. This force results from Reynolds stresses created by the buoyancy-driven convection.

The bubbles are effective for drag reduction only in flows with small Re, since stronger flows wash them away. Explicit analysis of a sinusoidal heating pattern shows an increase of drag reduction proportional to Ra_p^2 and reaching up to 87 % of the isothermal reference value at $Ra_p = 5000$. This increase saturates when the heating becomes too extreme as additional flow structures are formed in the flow, increasing the overall dissipation. Only heating patterns corresponding to the heating wavenumber $\alpha = O(1)$ generate drag reduction that is of practical interest. The drag-reducing effect decreases proportionally to α^4 when the heating wavenumber becomes too small and to α^{-7} when the heating wavenumber becomes too large. This decrease correlates with the decrease of the strength of the natural convection and, thus, with the decrease in the magnitude of the Reynolds stresses. It is expected that a more effective drag

https://doi.org/10.1017/jfm.2012.465 Published online by Cambridge University Press

reduction could be achieved by optimizing heating patterns, including using three-dimensional patterns, and insulating the unheated wall to prevent escape of the heat.

REFERENCES

BARTHLOTT, W. & NEINHUIS, C. 1977 Purity of sacred lotus, or escape from contamination in biological surfaces. *Planta* **202**, 1–8.

DANIELLO, R., WATERHOUSE, N. E. & ROTHSTEIN, J. P. 2009 Turbulent drag reduction using superhydrophobic surfaces. *Phys. Fluids* **21**, 085103.

FLORYAN, J. M. 2012 The thermo-superhydrophobic effect. *Bull. Am. Phys. Soc.* **57** (1), X50.00015.

GAO, L. & MCCARTHY, T. J. 2006 A perfectly hydrophobic surface ($\theta(A)/\theta(R) = 180°/180°$). *J. Am. Chem. Soc.* **128**, 9052–9053.

JOSEPH, P., COTTIN-BIZONNE, C., BENOIT, J. M., YBERT, C., JOURNET, C., TABELING, P. & BOCQUET, L. 2006 Slippage of water past superhydrophobic carbon nanotube forests in microchannels. *Phys. Rev. Lett.* **97**, 156104.

KRISHNAN, M., UGAZ, V. M. & BURNS, M. A. 2002 PCR in a Rayleigh–Bénard convection cell. *Science* **298**, 793.

MARTELL, M., PEROT, J. B. & ROTHSTEIN, J. P. 2009 Direct numerical simulations of turbulent flows over superhydrophobic surfaces. *J. Fluid Mech.* **620**, 31–41.

MOHAMMADI, A. & FLORYAN, J. M. 2011 Pressure losses in grooved channels, *ExpertSystems in Fluid Dynamics Research Laboratory Report* ESFD-4/2011, Department of Mechanical and Materials Engineering, The University of Western Ontario.

MOHAMMADI, A. & FLORYAN, J. M. 2012 Mechanism of drag generation by surface corrugation. *Phys. Fluids* **24**, 013602.

OU, J., PEROT, J. B. & ROTHSTEIN, J. P. 2004 Laminar drag reduction in microchannels using ultrahydrophobic surfaces. *Phys. Fluids* **16**, 4635.

OU, J. & ROTHSTEIN, J. P. 2005 Direct velocity measurements of the flow past drag-reducing ultrahydrophobic surfaces. *Phys. Fluids* **17**, 103606.

QUÉRÉ, D. 2008 Wetting and roughness. *Annu. Rev. Mater. Res.* **38**, 71–99.

REYSSAT, M., YEOMANS, J. M. & QUÉRÉ, D. 2008 Impalement of fakir drops. *Europhys. Lett.* **81**, 26006.

ROTHSTEIN, J. P. 2010 Slip on superhydrophobic surfaces. *Annu. Rev. Fluid Mech.* **42**, 89–109.

SAMAHA, M. A., TAFRESHI, H. V. & GAD-EL-HAK, 2011 Modelling drag reduction and meniscus stability of superhydrophobic surfaces comprised of random roughness. *Phys. Fluids* **23**, 012001.

TRUESDELL, R., MAMMOLI, P., VOROBIEFF, P., VAN SWOL, P. & BRINKER, C. J. 2006 Drag reduction on a patterned superhydrophobic surface. *Phys. Rev. Lett.* **97**, 044504.

XI, Z., FENG, S., JIA, N., YUGUI, J. & ZHIQIANG, W. 2008 Superhydrophobic surfaces: from structural control to functional application. *J. Mater. Chem.* **18**, 621–633.

ZHOU, M., LI, J., WU, C., ZHOU, X. & CAI, L. 2011 Fluid drag reduction on superhydrophobic surfaces coated with carbon nanotube forest (CNTs). *Soft Matt.* **7**, 4391–4396.

https://doi.org/10.1017/jfm.2012.465 Published online by Cambridge University Press